Development and performance validation of a low-cost algorithms-based hyperspectral imaging system for radiodermatitis assessment

SHICHENG HAO,[1,†] YING XIONG,[1,†] SISI GUO,[1] JING GAO,[1] XIAOTONG CHEN,[2] RUOYU ZHANG,[2,3] LIHUI LIU,[1,4] AND JIANFENG WANG[1,5] (iD)

[1]*Key Laboratory of Photoelectronic Imaging Technology and System of Ministry of Education of China, School of Optics and Photonics, Beijing Institute of Technology, Beijing 100081, China*
[2]*School of Medical Technology, Beijing Institute of Technology, Beijing 100081, China*
[3]*ryzh@bit.edu.cn*
[4]*liulihui@bit.edu.cn*
[5]*wangjianfeng@bit.edu.cn*
[†]*Authors with equal contribution*

Abstract: Whilst radiotherapy (RT) is widely used for cancer treatment, radiodermatitis caused by RT is one most common severe side effect affecting 95% cancer patients. Accurate radiodermatitis assessment and classification is essential to adopt timely treatment, management and monitoring, which all depend on reliable and objective tools for radiodermatitis grading. We therefore, in this work, reported the development and grading performance validation of a low-cost (~2318.2 CNY) algorithms-based hyperspectral imaging (aHSI) system for radiodermatitis assessment. The low-cost aHSI system was enabled through Monte Carlo (MC) simulations conducted on multi-spectra acquired from a custom built low-cost multispectral imaging (MSI) system, deriving algorithms-based hyper-spectra with spectral resolution of 1 nm. The MSI system was based on sequentially illuminated narrow-band light-emitting diodes (LEDs) and a CMOS camera. Erythema induced artificially on healthy volunteers was measured by the aHSI system developed, with algorithms-based hyper-spectra and skin layer resolved physiological parameters (i.e., the blood volume fraction (BVF) and the oxygen saturation of hemoglobin in blood, et. al.) derivation using MC simulations. The MC simulations derived BVF and the oxygen saturation of hemoglobin in blood showed significant (P < 0.001, analysis of variance: ANOVA) increase with erythema. Further 1D-convolution neural network (CNN) implemented on the algorithms-based hyper-spectra leads to an overall classification accuracy of 93.1%, suggesting the great potential of low-cost aHSI system developed for radiodermatitis assessment.

1. Introduction

In 2022, 4,820,000 and 2,370,000 new cancer cases, and 3,210,000 and 640,000 cancer deaths were estimated to occur in China and the USA, respectively [1]. Killing cancer cells and/or inhibiting their growth through high-energy radiation [2], radiotherapy (RT) is one most important and widely adopted treatment. The established role RT plays is well recognized [2,3]. Yet, RT unavoidably causes series of adverse reactions including radiation dermatitis: an RT-caused skin inflammation that usually occurs when the RT-treated lesion is close to or penetrates the skin [4]. Radiation dermatitis is reported to occur in ~95% patients accepting RT, in the form of skin redness, pain, erosion, ulcer and other serious symptoms [4–6]. Currently, radiation dermatitis can be divided into three categories (i.e., erythema, dry desquamation, and moist desquamation), among which erythema is the most common symptom at the earliest stage, accounting for 90% of patients with radiation dermatitis [4,7]. If left unmonitored or untreated, radiation dermatitis

may lead to RT treatment interruption, and negatively affect the patient's posttreatment quality of life [7]. Therefore, accurate assessment and classification of radiation dermatitis is highly needed to ensure timely monitoring, and treatment (if found needed) thereof.

At present, the commonly used methods for the assessment and detection of radiation dermatitis mainly include observation of clinical signs, patient self-reports, subjective assessment by doctors, and measurement of biological and biophysical parameters of local skin [4,6]. However, these methods are found with certain limitations. For instance, subjective assessment by doctors not only increase their workload but may result in inter-doctor disagreement [6,8]. There is therefore unmet clinical need to develop objective methods for accurate assessment and classification of radiation dermatitis. Various methods and imaging modalities (i.e., OCT: optical coherence tomography [9–11], confocal microscopy and digital dermoscopy [12–15], photoacoustic imaging [16], and Raman spectroscopy [17], et. al.) have been developed. Among these, Photiou [9] et al. reported OCT in combination with machine learning for the differentiation between normal skin and early-stage radiation dermatitis. Based on confocal microscopy and digital dermoscopy readings, Kišonas [12] et al. proposed an assessment scale to reflect the severity of radiation dermatitis of 103 breast patients receiving RT. Exploring the biochemical changes associated with radiation dermatitis, Hariri [16] et al. and Kanemura [17] et al. explored the suitability of photoacoustic imaging and Raman spectroscopy, respectively, for erythema identification with promising results. While the above-mentioned methods demonstrate great potential for objective radiation dermatitis assessment, their field of view (FOV) is relatively limited at a few millimeters, making it challenging for them to assess large-area radiation dermatitis.

Exploring both the morphology and biochemical information of the investigated samples at large FOV, multispectral imaging (MSI) and hyperspectral imaging (HSI) are actively explored for skin investigation. For instance, Bjorgan [18] et al. obtained hyperspectral images of human skin covering the wavelength range of 400-1000 nm. Also, they proposed an algorithm based on an inverse Monte Carlo model to decompose the hyperspectral data and extract biological parameter information from the skin samples, demonstrating the suitability of HSI to derive physiology relevant parameters from the skin. More recently, Abdlaty [8] et al. reported HSI imaging study of induced erythema on three volunteers, showing that HSI imaging could accurately differentiate different-graded erythema. Compared with HSI requiring relatively complicated and cost hardware setups, simplified and more affordable MSI imaging based on sequentially - illuminated narrow-band light-emitting diodes (LEDs) and CMOS camera have also been investigated, in parallel, for skin investigation (Bernat [19] et al, and Bolton [20] et al.). In particular, Monte Carlo (MC) simulations implemented on MSI spectra could not only derive algorithms-based HSI spectra that closely resemble traditional HSI spectra, but also physiological meaningful parameters (e.g., blood oxygen saturation and melanin content et.al.) from the skin. Yet, previously reported work [20] only evaluated the suitability of algorithms-based HSI derivation from MSI spectra on Caucasian volunteers. In addition, the MSI system cost is to be further lowered, making it more affordable even for low-resource settings. Therefore, in this paper, we reported the development and grading performance validation of a low-cost (~2318.2 CNY, which is three times lower than that by Bolton et al [20]) algorithms-based hyperspectral imaging (aHSI) system for radiodermatitis assessment on more general populations. The LED lighting arrangement for uniform - and the synchronization control based on STM32 for sequential-illumination were detailed. Theory and Python code for MC simulations enabling algorithms-based hyper-spectra generation from multi-spectra were also described in detail. Besides, analysis of variance (ANOVA) was implemented on the MC derived physiological relevant parameters to reveal the associated parameters accompanying erythema, followed by 1D-convolution neural network (CNN) based classification of algorithms-based hyper-spectra acquired from the normal skin and the skin with erythema, thereby validating the performance of the system developed for radiodermatitis assessment.

2. Experimental methods

2.1. MSI Hardware System based on Sequentially-illuminated LEDs and a Single CMOS Camera

The schematic diagram of the low-cost MSI system developed is shown in Fig. 1(a). The system mainly consists of an LED (BoYaKeJi, Shenzhen, China) array for illumination, a black-and-white CMOS camera (HIKROBOT, Hangzhou, China) for imaging, STM32 microcontroller (STM32F103, ST, Italy and French) and relays (BMZ-R1-E, SongChuan, Shanghai, China) to realize sequential LED illumination, and a computer for multi-spectra image acquisition, processing and display under sequential LED illumination. Eleven I/O ports of the STM32 microcontroller (Fig. 1(a)) were used in synergy with relays (Fig. 1(a)) to turn on/off the eleven LEDs (Fig. 1) covering 420 - 660 nm sequentially, and the twelfth I/O port controls the CMOS image capture at each wavelength. The center wavelengths and full width at half maximum (FWHM) of all LEDs were determined using a commercial spectrometer (Aurora4000, CNI, Changchun, China) and included in Table 1. Also included in Table 1 were the operating voltages and the input electrical power as provide by the manufactures, and the output optical power measured using an optical power meter (PM100D, Thorlabs, USA).
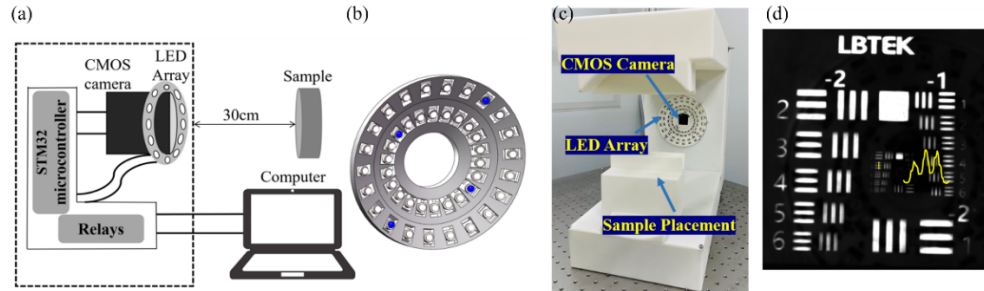

Fig. 1. (a) Schematic diagram of the multi-spectral imaging (MSI) system developed. (b) LED arrangement illustration. (c) Picture of the real MSI system developed. (d) The spatial resolution is 0.445 mm. The blue-color indicated LEDs in (b) illustrates typical LED arrangement for uniform illumination.

Table 1. Specifications of the LEDs used

LED Number	Central wavelength (nm)	FWHM (nm)	Operating voltage (V)	Input electrical power(W)	Output optical power(μW)
1	428.514	18.99	3.3	3	74
2	441.989	20.06	3.3	3	134
3	471.745	28.26	3.3	3	83
4	505.012	30.52	3.3	3	76
5	530.783	31.80	3.3	3	120
6	544.957	43.10	3.3	3	14
7	571.161	48.17	3.3	3	17
8	591.034	15.31	2.5	3	6
9	598.672	15.74	2.5	3	7
10	619.989	16.04	2.5	3	29
11	666.628	18.79	3.3	3	156

One notes that the beam angle of each LED is 60 degrees, covering a solid angle range of π. Considering the 3D feature of the skin under investigation and uniform illumination needed, 4 LEDs covering 4 quadrants were adopted at each wavelength (Fig. 1(b)), resulting in a total of 44 LEDs in the LED array. The real MSI system developed was pictured in Fig. 1(c). As shown, the lens was adjusted to the optimal working distance of 30 cm, the diameter of resultant FOV is 25 cm × 20 cm, making it feasible to acquire MSI spectra from wide skin area. Also, a sample placement holder (Fig. 1(c)) was added to ensure consistent MSI spectra positioning. The spatial resolution is 0.445 mm (Fig. 1(d)), determined by using a USAF 1951 resolution target (RTS3AB-N, LBTEK, Shenzhen, China). The overall cost of the system is ~2318.2 CNY (Table 2), making it affordable for low-resource settings.

Table 2. Component list of the low-cost MSI system developed

Component	Vendor	Cost (CNY)
CMOS camera (X1)	HIKROBOT, Hangzhou, China	650
Camera lens (X1)	HIKROBOT, Hangzhou, China	508
LEDs (X11)	BoYaKeJi, Shenzhen, China	193
Microcontroller (X1)	STM32F103, ST, Italy and French	178
Relays (X4)	BMZ-R1-E, SongChuan, Shanghai, China	427.2
3D printed mount (X1)	HebeiZhizao, Shijiazhuang, China	362
Total:	(-)	2318.2

The time diagram for sequential LED illumination and image capture at each wavelength is shown in Fig. 2. Specifically, the frequency of the clock signal (CLK as in Fig. 2) from the microcontroller was 1kHz. Before the onset of each MSI spectra acquisition, the microcontroller was switched on for 3 seconds, then the I/O port controlling the first LED (LED1, Fig. 2) emits a high-level TTL signal (time period of 19.5s, duty cycle of 7.7%. LED1 Trigger as in Fig. 2) that was transferred to the relay (Fig. 1(a)), turning on the first LED for 1500 ms. Empirical experimental results showed a total of 8 images captured during the LED 'on' period would guarantee best signal to noise ratio (SNR), as will be validated below (in Sec. 2.2 and Sec. 3.1). One notes that there was a time period of 150 ms both before and after the 8 images capture, during which the CMOS exposure was rising edge triggered with exposure time set at 140 ms followed by 10 ms for timely image transfer (Images Acquisition Trigger, Fig. 2), thereby avoiding captured images cross-talk under different LED illuminations. Thereafter, the remaining 10 LEDs trigger signals (LED2 Trigger, ..., LED11 Trigger, Fig. 2) were generated by the STM32 microcontroller with a time delay of 1500 ms. In the meanwhile, the image acquisition triggers for synchronized CMOS image capture under the 10 LEDs illumination were sequentially generated with the same specs as that LED1. A total of 19.5s was needed for MSI spectra acquisition. The code sent to STM32 controller for controlling the time sequences was included as supplemental materials (Code 1) [21].

To evaluate the thermal stability of the LEDs used (Table 1), the output LED spectra were acquired within 1200 ms at three intervals corresponding to the image capture period (Fig. 2), using the commercial spectrometer (Aurora4000, CNI, Changchun, China). One notes that the spectrometer can be externally and rise-edge signal triggered. Therefore, within each 1200 ms of the image acquisition, a square wave signal (period of 400 ms and duty cycle of 50%, Spectra Acquisition Trigger, Fig. 2) from the microcontroller was sent to the spectrometer for synchronization. The light from LEDs collected by a fiber probe fixed on the sample placement of the MSI system developed (Fig. 1 (c)). For each LED, a set of three spectra were finally recorded and analysed to quantify the LED thermal stability.
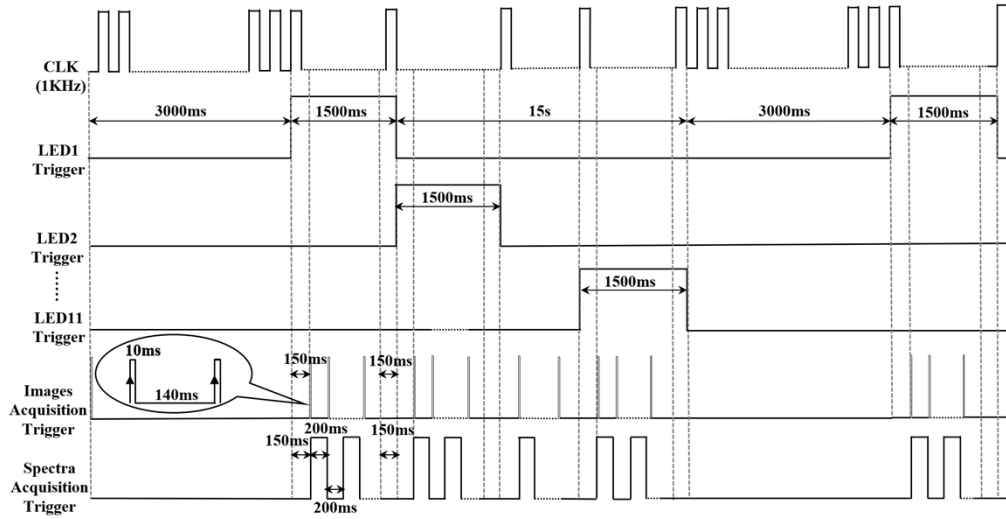
Fig. 2. The time diagram for sequential LED illumination, CMOS camera image capture and spectra capture at each wavelength.

2.2. Multi-spectra processing and MSI system performance validation

Before taking the sample MSI measurement under sequential LED illumination ($I_{\lambda,sample}$), the dark frame image for sample($I_{dark,sample}$) and white standard board ($I_{dark,white_{std}}$) were captured ahead when all LEDs were switched off at the very beginning of the first 3000 ms (Images Acquisition Trigger, Fig. 2) during each image capture cycle. After the MSI measurement ($I_{\lambda,white_{std}}$) of a diffuse reflectance standard (WS-1, Ocean Insight, Orlando, Florida) under sequential LED illumination, the multi-spectra (R_λ) could be derived as below:

$$R_\lambda = \frac{I_{\lambda,sample} - I_{dark,sample}}{I_{\lambda,white_{std}} - I_{dark,white_{std}}} \tag{1}$$

To validate the performance of the MSI system developed (Fig. 1), we compared the measurements of a standard 24-color chart (Datacolor Spyder, USA) using both a commercial spectrometer (Aurora4000, CNI, Changchun, China) and the MSI system developed. The experimental setup taking the standard diffuse reflectance spectrum of the color chart was shown in Fig. 3. Briefly, a fiber probe with two SMA905 connector-terminated input ends and one common output end is vertically fixed on a horizontal bracket. White light from a 3W white-light LED (BoYaKeJi, Shenzhen, China) was sent to one SMA905 connector, incident onto- and back-scattered from the color chart, and then detected by the spectrometer. The distance between the fiber probe tip and the color chart was fixed at 2 mm. In order to acquire the DRS from the whole color chart, the color chart was moved to measure diffusely reflected signal from each of its 24 color blocks. After that, the DRS spectrum of the whole color chart was obtained through its division by the reflected signal averaged overall the central 10 mm diameter region of the chart. Further, using the color chart as example, we have set different number of images (i.e., 2, 4, 6, 8) captured to derive the MSI spectra with highest SNR while considering the overall acquisition time. The mean square error (MSE) between the MSI spectra and the spectrometer-measured DRS spectrum was calculated, and that with lowest MSE was considered optimal.
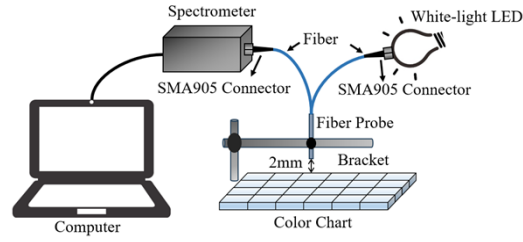
Fig. 3. Diffuse reflectance spectrum measurement of a standard color chart using a commercial spectrometer.

2.3. Monte Carlo simulation based low-cost aHSI system development and skin layer resolved physiological parameters derivation

The low-cost aHSI system was enabled through Monte Carlo (MC) simulations conducted on multi-spectra acquired from the custom built low-cost MSI system (Fig. 1(c)). In parallel, MC simulations allowed extraction of physiological meaningful parameters from the skin MSI spectra measured. Specifically, we have built the MC Lookup table (MCLUT) to convert the multi-spectra to algorithms-based hyper-spectra. Slight modifications were made to fit our simulations on a six-layer skin model [20] from publicly available python code [22]. Specially, the algorithms-based hyper-spectra were determined through feeding to our modified MC code the layer-resolved absorption coefficient (μ_a), scattering coefficient (μ_s) and layer thickness (Table 3).

Table 3. Name and thickness of each skin layer for MCLUT built-up

Layer name	Layer thickness (μm)
Epidermis	50
Basal layer	10
Papillary dermis	250
Dermal venous plexus	50
Reticular dermis	1×10^4
Subcutaneous Tissue	5×10^4

The layer-resolved μ_a and μ_s were determined as [20,23]:

$$\mu_a(\lambda) = BVFS\mu_{a,oxy}(\lambda) + BVF(1-S)\mu_{a,deoxy}(\lambda) + W\mu_{a,water}(\lambda) + M\mu_{a,melanosome}(\lambda) + \sum_i f_i\mu_{a,i}(\lambda) \tag{2}$$

where BVF is the blood volume fraction, S is the oxygen saturation of hemoglobin, W is the water volume, M is the volume fraction of typical cutaneous melanosomes in the epidermis and basal layer, f_i and $\mu_{a,i}(\lambda)$ are the volume fraction and absorption coefficient of any additional absorber in these tissue [20], respectively.

The value and variation for BVF, S, W, M of each skin tissue layer are included in Table 4, showing that the three most prominent parameters suitable for Asian volunteers are: M of the epidermis and basal layer; BVF and S of the dermal venous plexus. Furthermore, according to *Lambert-Beer* Law [24], the absorption coefficients of oxy-hemoglobin [$\mu_{a,oxy}(\lambda)$] and deoxy-hemoglobin [$\mu_{a,deoxy}(\lambda)$] in whole blood as involved in Eq.(2) could be derived as below:

$$\mu_{a,oxy}(\lambda) = \frac{2.303 \times HbO_2 \times \lambda}{64500} \tag{3}$$

$$\mu_{a,deoxy}(\lambda) = \frac{2.303 \times Hb \times \lambda}{64500} \tag{4}$$

where HbO_2 is the molar extinction coefficient of oxy-hemoglobin, and Hb is the molar extinction coefficient of hemoglobin, and their wavelength-dependent values are from Prahl [24].

Table 4. The parameter variation range of each skin layer as adopted in the MC simulation

Layer	BVF	S	M	W	μ'_{s500nm}	f	b_{Mie}	g
Epidermis	0	0.75	0.009~0.036	0.75	40	0	1	0.9
Basal layer	0	0.75	0.036~0.144	0.75	40	0	1	0.9
Papillary dermis	0.0005	0.55	0	0.65	30	0.62	0.91	0.9
Dermal venous plexus	0.045~0.18	0.63~0.99	0	0.75	10	0.62	0.91	0.9
Reticular dermis	0.0005	0.55	0	0.65	30	0.62	0.91	0.9
Subcutaneous tissue	0.05	0.55	0	0.75	10	0.6	0.9	0.9

The absorption coefficient of water [$\mu_{a,water}(\lambda)$] and melanosome [$\mu_{a,melanosome}(\lambda)$] as involved in Eq.(2) could be calculated by Eq. (5) [25] and (6) [26] below, respectively:

$$\mu_{a,water}(\lambda) = \frac{4\pi n''}{\lambda} \tag{5}$$

$$\mu_{a,melanosome}(\lambda) = 679.16 \left(\frac{\lambda}{500} \right)^{-3.33} \tag{6}$$

where n'' is the imaginary refractive index of water [25].

Moreover, the μ_s could be calculated by Eq. (7) and Eq. (8):

$$\mu_s'(\lambda) = \mu'_{s500nm} \left[f \left(\frac{\lambda}{500} \right)^{-4} + (1-f) \left(\frac{\lambda}{500} \right)^{-b_{Mie}} \right] \tag{7}$$

$$\mu_s(\lambda) = \frac{\mu_s'(\lambda)}{1-g} \tag{8}$$

where the $\mu_s'(\lambda)$ is the reduced scattering coefficient, the μ'_{s500nm} is the reduced scattering at 500 nm, f is the fraction of Rayleigh scattering, $(1-f)$ is the fraction of Mie scattering, b_{Mie} is the scattering power of Mie scattering, and g is the anisotropy of scattering. Similarly, μ'_{s500nm}, f and b_{Mie} of each skin tissue layer variation are also included in Table 4.

In our study, the algorithms-based hyper-spectra cover the wavelength range of 420 nm to 660 nm, but could be easily extended to near-infrared wavelength range. The resolution of the algorithms-based hyper-spectra was 1 nm as determined by the wavelength interval set for MC simulation, corresponding to 240 pixels for the algorithms-based hyper-spectra as reported in our work. While it took nearly a week to build the MCLUT as used in this work, the searching time for a best fit algorithms-based hyper-spectra to the MSI spectra was less than 0.1s. The MSE between the algorithms-based hyper-spectra and the multi-spectra measured was calculated, and the algorithms-based hyper-spectra with minimum MSE were selected. Thereafter, the corresponding physiological parameters set were also derived.

2.4. Erythema model and validation study design

To demonstrate the system's capability for radiation erythema identification and grading, we intentionally induced skin erythema on three Asian volunteers to simulate the radiation erythema effects. The erythema was induced through ~3 minutes striking of the palm using a plastic ruler. There was no obvious degrading of erythema during the first five minutes, and almost
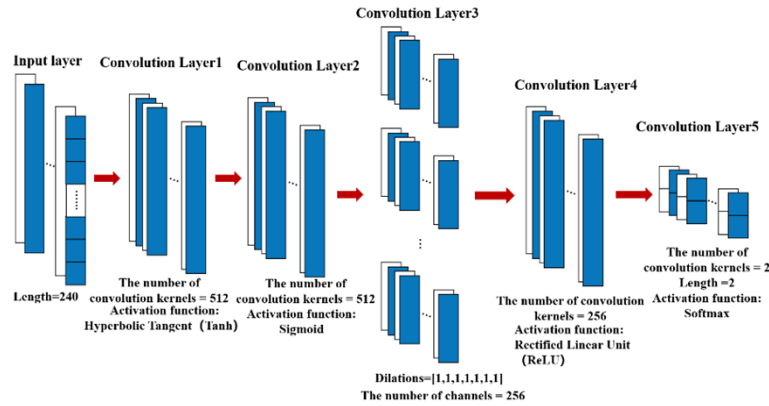
Fig. 4. Schematic of 1D-CNN model developed used in this study (kernel size = 5, strid = 1, padding = same) for algorithms-based hyper-spectra classification.

disappeared after 40 minutes, ensuring stable MSI spectra measurement from the erythema induced. Following the steps below, the multi-spectra before and after erythema induction could be derived within 5 minutes for each volunteer:

Step #1, a diffuse reflectance standard (WS-1, Ocean Insight, Orlando, Florida) was placed on the sample placement holder (Fig. 1(c)), then the MSI system captured the dark frame image of the diffuse reflectance standard whiteboard ($I_{dark,white_{std}}$) and the images at each wavelength ($I_{\lambda,white_{std}}$), followed by the whiteboard removal.

Step #2, the palm before erythema induction was placed on the sample placement holder (Fig. 1(c)), a black marker pen defined the palm region of interest (ROI) sized 3 cm × 3 cm, and the dark frame image of the palm($I_{dark,sample}$) and the images at each wavelength ($I_{\lambda,sample}$) of the palm were captured.

Then the MSI spectra of the palm before erythema induction could be derived using Eq. (1). Repeating the steps above, the MSI spectra of the skin after erythema induction could also be derived.

Thereafter, the algorithms-based hyper-spectra and skin-layer resolved physiological parameters associated with normal skin and erythema could be derived using the MCLUT built (Sec. 2.3).

2.5. Statistical analysis

To evaluate the performance of the low-cost aHSI system developed for skin erythema identification, analysis of variance (ANOVA) were implemented on physiological parameters (*BVF*, *S* and *M* as in Table 4) derived. 1D convolutional neural networks (1D-CNN) based binary classification of algorithms-based hyper-spectra were also conducted. Figure 4 showed the 1D-CNN model we built. In this model, the length of input and output layer is 240 and 2, respectively, corresponding to the 240 wavelengths of the algorithms-based hyper-spectra, and the 2 categorical series (normal and erythema). In total, 24000 (normal: 12000, erythema: 12000) algorithms-based hyper-spectra were extracted from the three volunteers recruited, and the associated 24000 sets of physiological parameters (*BVF*, *S* and *M*) were analysed. Each volunteer's ROI region contains more than 10000 pixels, and we randomly sampled 4000 pixels from each ROI region to obtain the data. 80% of the algorithms-based hyper-spectra were used as the training set to train the 1D-CNN network structure, while the remaining 20% spectra served as the validation set to validate the training results. We performed maximum normalization on all spectral data to highlight spectral features, and used an NVIDIA GeForce RTX 3060 armed GeekPro computer (Lenovo, Beijing, China) for both training and validation. The network of 1D-CNN in this study

is a fully convolutional network, which the fully connected layer was converted into convolutional layers (Convolution Layer4 and Convolution Layer5 shown in Fig. 4). An epoch number of 50 was found sufficient to ensure training and validation accuracies higher than 0.9. The loss is calculated according to the function (tf.nn.sparse_softmax_cross_entropy_with_logits()) in the tensorflow library. Moreover, we selected the Adaptive Moment Estimation (Adam) optimizer (tf.train.AdamOptimizer()) to optimize the parameter optimization, which can learn adaptively according to the loss value, and adjust the correction angle according to the size of the loss when running the program. The optimized network structure was found to achieve a better classification effect. 50 set of spectra were input for training at a time. The total training and validation time was about 4.5 hours, and the time of classification for one set of spectral data was about 4s. Based on the validation results, the receiver operating characteristic (ROC) curve, sensitivity, specificity, and accuracy were also derived to validate the discriminative ability of the aHSI system we developed for normal skin and radiation dermatitis evaluation.

3. Results and discussion

To evaluate the reliability of the aHSI system developed, we firstly assessed the thermal stability of the LEDs (Sec. 3.1), and assessed the performance of the MSI system (Fig. 1(c)) based on which algorithms-based hyper-spectra are derived (Sec. 3.2), followed by accuracy estimation of algorithms-based hyper-spectra (Sec. 3.3). Thereafter, the algorithms-based hyper-spectra differences associated with normal skin and skin erythema were analysed (Sec. 3.4).

3.1. Thermal stability analysis of the LEDs

Figure 5 showed the thermal stability analysis results of the 11 LEDs utilized (Table 1). The recorded spectra overall demonstrated all 11 LEDs were stable during the MSI spectra acquisition. Further coefficient of variation (CV) analysis of the LED central wavelength and their relevant intensities lead to CVs within 0.09 and 0.54, confirming the thermal stability of all LEDs (Table 1).
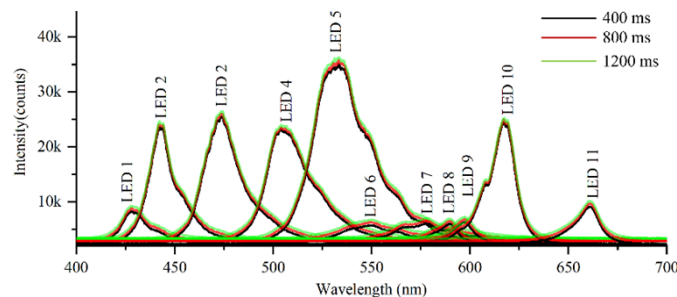

Fig. 5. The recorded LED spectra at 400 ms, 800 ms, and 1200 ms respectively. The spectra at 800 ms and 1200 ms were shifted by 500 and 1000, for better illustration.

3.2. Performance validation of MSI system

Using the real picture of a real the 24-color chart (Datacolor Spyder, USA) as background, Fig. 6 showed the multi-spectra (pink discrete balls) and diffuse reflectance spectra (blue continuous line, Fig. 6) taken and the MSE between them, respectively, using the MSI system developed and a commercial spectrometer in the wavelength range of 420-660 nm. As shown, it was evident that the spectral trends from both systems exhibited high consistency with MSE < 0.0058, thereby validating the reliability of the MSI system we developed (Fig. 1).
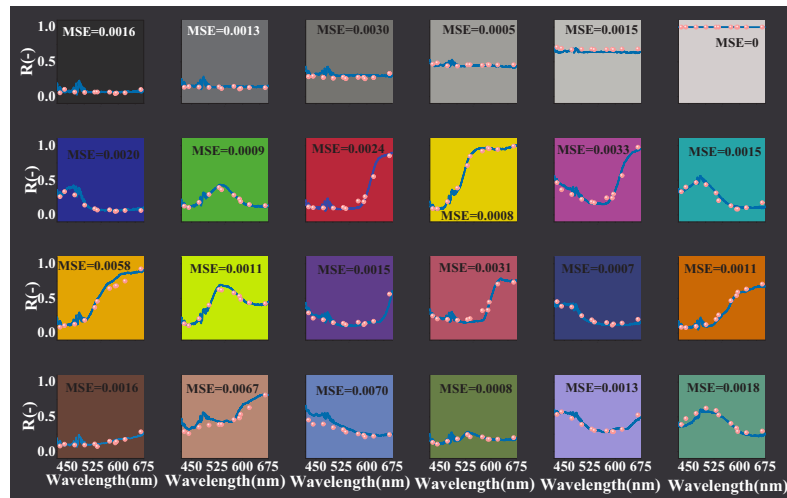
Fig. 6. Multi-spectra (pink discrete balls) and diffuse reflectance spectra (blue continuous line) taken using the MSI system developed and a commercial spectrometer, with MSE between them, both in the wavelength range of 420-660 nm.

Using the color chart as sample, we further investigated the MSE changes with different number of images captured. Figure 7 showed the typical results for its bright yellow block (located at the second row and the fourth column of the color chart, as in Fig. 6). When the captured image number increased from 2 to 8, the MSE were reduced from 0.0055 to 0.0008. Similar MSE change trends were noticed for other blocks of the color chart (data not shown). One notes that further increase of the captured image number will lead to an even smaller MSE. Yet, the MSI spectra acquisition time will be increased too. To balance a minimum MSE desired and fast MSI spectra acquisition, the captured image number was set as 8.
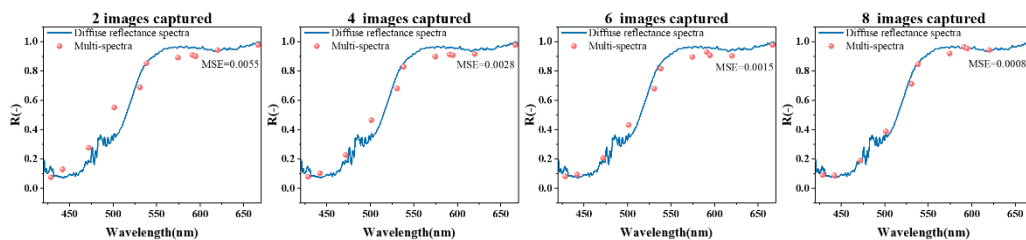

Fig. 7. MSE between the multi-spectra and the diffuse reflectance spectra with different number (2, 4, 6, 8) of images captured. A minimum MSE of 0.0008 was achieved when the number was set as 8.

3.3. Accuracy estimation of algorithms-based hyper-spectra

Figure 8(a) depicted the ROI on the volunteers' normal palm skin, and Fig. 8 (b) presented the typical multi-spectra obtained from normal skin along with the corresponding algorithms-based hyper-spectra, indicating good alignment between the two. Further quantitative analysis shows that the MSE between the multi-spectra and algorithms-based hyper-spectra were 0.54%, 0.36%, and 0.23%, respectively, for the spectra shown in Fig. 8, confirming the high accuracy of the algorithms-based hyper-spectra. In addition, for the total 12000 multi-spectra and algorithms-based hyper-spectra in the ROIs of the 3 volunteers, the mean ±1 standard deviation (SD) of MSE

was $0.56\% \pm 0.29\%$, reconfirming the accuracy of the algorithms-based hyper-spectra. Besides, one notes that unlike multi-spectra lacking absorption peaks at 540 nm and 575 nm, the two absorption peaks were evident in the algorithms-based hyper-spectra, showing the superiority of the algorithms-based hyper-spectra for deriving physiological parameters associated with hemoglobin. Similarly, the results of skin erythema were shown in Fig. 9. As consistent with results of normal skin, the MSE between the multi-spectra and algorithms-based hyper-spectra were 1.07%, 0.41%, and 0.34%, respectively, for the spectra shown in Fig. 9, whilst the mean ±1 standard deviation (SD) of the MSE calculated over all the algorithms-based hyper-spectra was $0.94\% \pm 0.55\%$, affirming the high accuracy of the algorithms-based hyper-spectra.
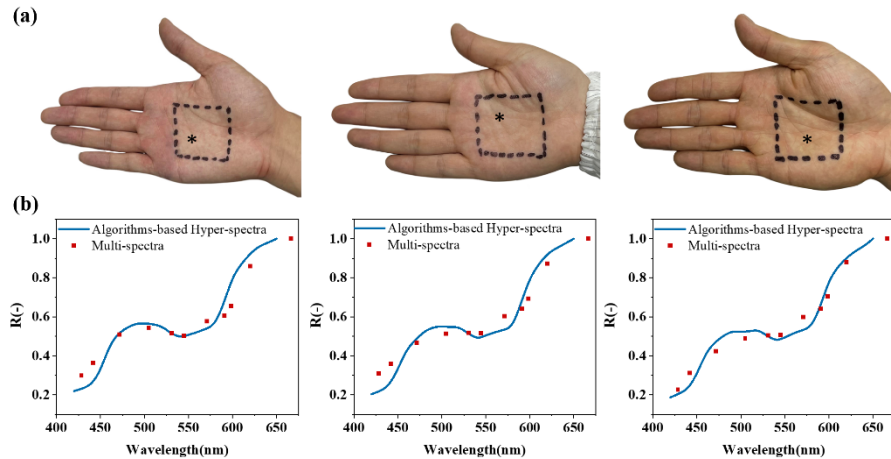

Fig. 8. (a) Picture of normal palm skins of the three healthy volunteers from which MSI images and multi-spectra were acquired. (b) Representative multi-spectra and algorithms-based hyper-spectra derived. The * indicated area where multi-spectra were selected.
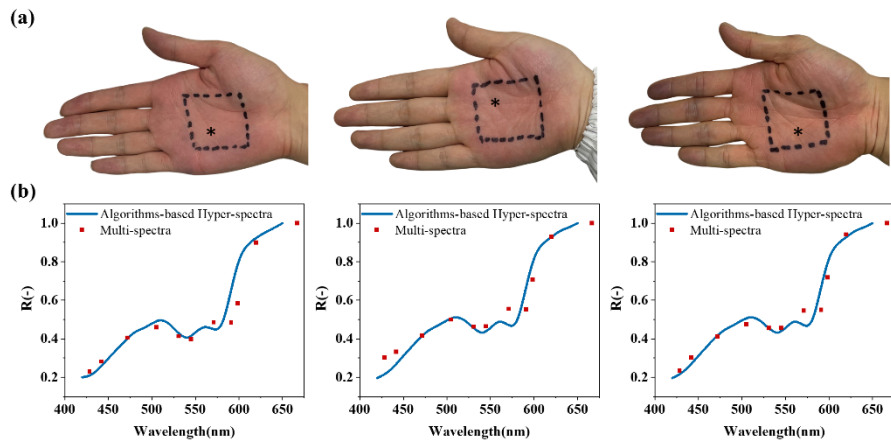

Fig. 9. (a) Picture of palm erythema of the three healthy volunteers from which MSI images and multi-spectra were acquired. (b) Representative multi-spectra and algorithms-based hyper-spectra derived. The * indicated area where multi-spectra were selected.

3.4. Analysis of algorithms-based hyper-spectra differences associated with normal skin and skin erythema

Fig.10a displayed the algorithms-based hyper-spectra of normal skin and skin erythema, and their algorithms-based hyper-spectra difference were shown in Fig. 10(b). Overall, the algorithms-based hyper - spectra of both the normal skin and skin erythema are dominated by absorption bands at 540 nm and 575 nm that could be attributed to oxygenated hemoglobin absorption. We have found the decreased algorithms-based hyper-spectra of hemoglobin band for the skin erythema, signifying the increased hemoglobin content associated with skin erythema. The increased hemoglobin content for skin erythema could be attributed to the increased supply in skin erythema. The hemoglobin content observed and the differences spectra (Fig. 10(b)) indicates capability of the algorithms-based hyper - spectra for skin erythema detection.
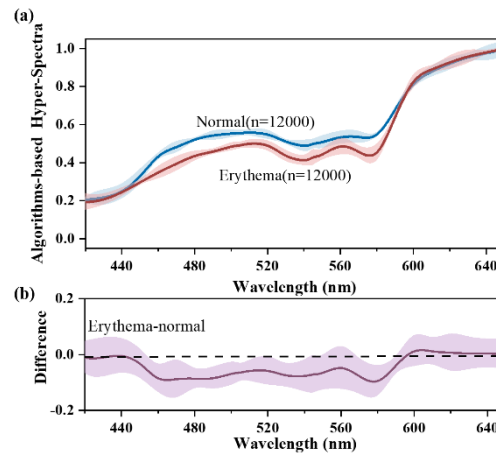

Fig. 10. (a) Mean ±1 standard deviation (SD) of algorithms-based hyper-spectra association with normal skin and skin erythema. (b) Algorithms-based hyper-spectra difference between normal skin and skin erythema.

To specify the biochemical basis for the algorithms-based hyper-spectra difference observed, the relative contribution of the volume fraction of typical cutaneous melanosomes (M) in the epidermis and basal layer, together with the blood volume fraction (BVF) and the oxygen saturation(S) of hemoglobin of dermal venous plexus, associated with normal skin and skin erythema were plotted in Fig. 11. As shown, significant ($P < 0.001$, ANOVA) increased blood supply was found for skin erythema, as consistent with algorithms-based hyper-spectra derived. Intriguingly, we also noticed the relative contribution of melanosomes was higher with skin erythema, observation that is consistent with previous studies [27,28] that reveal increased melanosome accompanying erythema of colored volunteers using DRS. MC simulation based algorithms-based hyper-spectra as we reported herein could not only reveal gross spectra differences between normal skin and erythema (Fig. 10), but also elucidate physiological component changes thereof (Fig. 11), laying the foundation of using algorithms-based hyper-spectra for radiodermatitis assessment.

Whist results in Fig. 10 and Fig. 11 demonstrated the capability of the aHSI developed for skin erythema detection, we further quantified the classification accuracy using the algorithms-based hyper-spectra based on 1D-CNN. Figure 12(a) showed the posterior probabilities of algorithms-based hyper - spectra belonging to (i) normal skin (n = 2400), and (ii) skin erythema (n = 2400), with sensitivity of 99.6% (2390/2400), specificity of 86.7% (2080/2400), and an overall accuracy of 93.1% (4470/4800). The receiver operating characteristic (ROC) curve is also generated (Fig. 12(b)), with the integration area under the ROC curve (AUC) of being
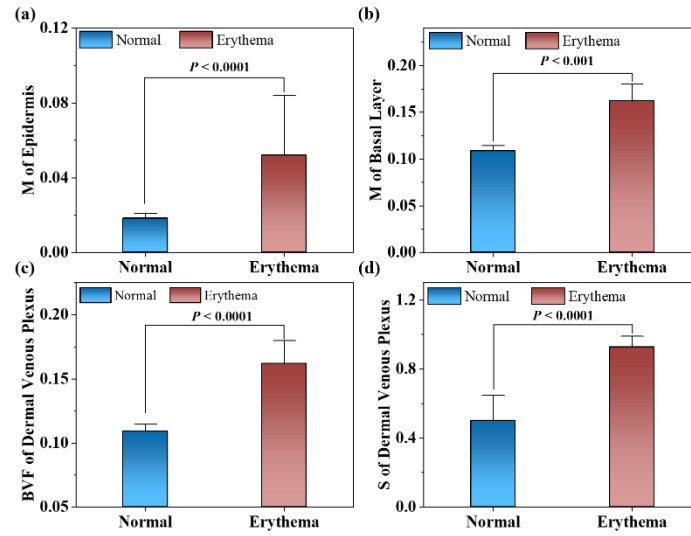
Fig. 11. Bar diagrams ±1 SD showing the distribution of the cutaneous melanosomes volume fraction (M) of epidermis (a) and basal layer (b), the blood volume fraction (BVF) (c) and the oxygen saturation(S) of hemoglobin (d) dermal venous plexus.

0.99. The quantitative results in Fig. 12 confirm that low-cost aHSI system developed and the algorithms-based hyper-spectra generated provide a best detection performance for skin erythema.
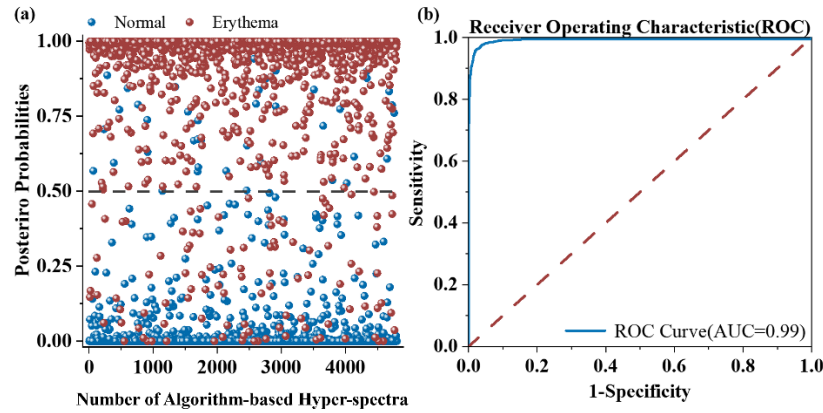

Fig. 12. (a) The posterior probabilities of algorithms-based hyper - spectra belonging to (i) normal skin (n = 2400), and (ii) skin erythema (n = 2400) of the validation dataset (20% of the total dataset), using 1D-CNN. (b) Receiver operating characteristic (ROC) curves for separating skin erythema from normal skin for the validation dataset (20% of the total dataset). The area under the ROC curve (AUC) was 0.99 using the algorithms-based hyper-spectra.

4. Conclusion

We have detailed the development of a low-cost algorithms-based hyperspectral imaging (aHSI) system that could be used for radiodermatitis assessment. The accuracy of the aHSI system have been fully evaluated on three Asian volunteers, generating algorithms-based hyper-spectra that

could reveal physiological parameter (i.e., haemoglobin) changes associated with skin erythema. Capitalizing on the high-dimensional algorithms-based hyper-spectra, skin erythema could be differentiated with high accuracy of 93.1%, demonstrating the potential of the aHSI to become not only a non-invasive, rapid, and reliable but also an affordable diagnostic tool for quantitative radiation dermatitis assessment.

Disclosures. Ying Xiong initiated the hardware design of the MSI system developed. Shicheng Hao further optimized the system hardware, and was in charge of the system software development as reported in this work.

Data availability. The data that support the findings of this study are available from the corresponding author upon reasonable request, on a collaboration basis. The 1D-CNN and modified MCML code used in this paper are not publicly available, but can be shared in a collaborative manner.

References

1. C. Xia, X. Dong, H. Li, M. Cao, D. Sun, S. He, F. Yang, X. Yan, S. Zhang, and N. Li, "Cancer statistics in China and United States, 2022: profiles, trends, and determinants," Chin. Med. J. **135**(5), 584–590 (2022).
2. R. Baskar, J. Dai, N. Wenlong, R. Yeo, and K.-W. J. F. I. M. B. Yeoh, "Biological response of cancer cells to radiation treatment," Front. Mol. Biosci. **1**, 24 (2014).
3. L. Gong, Y. Zhang, C. Liu, M. Zhang, and S. Han, "Application of radiosensitizers in cancer radiotherapy," Int. J. Nanomedicine **16**, 1083–1102 (2021).
4. M. Singh, A. Alavi, R. Wong, and S. Akita, "Radiodermatitis: a review of our current understanding," Am. J. Clin. Dermatol. **17**(3), 277–292 (2016).
5. J. Ryan Wolf, C. E. Heckler, J. J. Guido, A. R. Peoples, J. S. Gewandter, M. Ling, V. P. Vinciguerra, T. Anderson, L. Evans, and J. Wade, "Oral curcumin for radiation dermatitis: A URCC NCORP study of 686 breast cancer patients," Support. Care Cancer **26**(5), 1543–1552 (2018).
6. S. Finkelstein, L. Kanee, T. Behroozian, J. R. Wolf, C. van den Hurk, E. Chow, and P. Bonomo, "Comparison of clinical practice guidelines on radiation dermatitis: a narrative review," Support. Care Cancer **30**(6), 4663–4674 (2022).
7. L. Drost, N. Li, D. Vesprini, A. Sangha, J. Lee, E. Leung, E. Rakovitch, C. Yee, E. Chow, and M. Ruschin, "Prospective study of breast radiation dermatitis," Clin. Breast Cancer **18**(5), e789–e795 (2018).
8. R. Abdlaty, L. Doerwald-Munoz, A. Madooei, S. Sahli, S.-C. A. Yeh, J. Zerubia, R. K. W. Wong, J. E. Hayward, T. J. Farrell, and Q. Fang, "Hyperspectral Imaging and Classification for Grading Skin Erythema," Front Phys. **6**, 72 (2018).
9. C. Photiou, I. Strouthos, C. Cloconi, and C. Pitris, "Early identification of low-grade acute radiation dermatitis using in vivo optical coherence tomography (OCT) images of human head and neck," Proc. SPIE **12367**, 1236713 (2023).
10. C. Photiou, I. Strouthos, and C. Cloconi, "In vivo early detection of acute radiation dermatitis using optical coherence tomography (OCT) images," Proc. SPIE **11948**, 1194801 (2022).
11. C. Photiou, I. Strouthos, and C. Cloconi, "Early Detection of Acute Radiation Dermatitis (ARD) Using In Vivo Optical Coherence Tomography (OCT) Images," in *Biophotonics Congress: Biomedical Optics 2022 (Translational, Microscopy, OCT, OTS, BRAIN)*, Technical Digest Series (Optica Publishing Group, 2022), paper CM2E.4.
12. J. Kisonas, J. Venius, M. Grybauskas, D. Dabkeviciene, A. Burneckis, and R. Rotomskis, "Acute Radiation Dermatitis Evaluation with Reflectance Confocal Microscopy: A Prospective Study," Diagn. **11**(9), 1670 (2021).
13. J. Kišonas, J. Venius, O. Sevriukova, M. Grybauskas, K. Guogytė, A. Burneckis, and R. Rotomskis, "Application of reflectance confocal microscopy for early diagnosis of radiation-induced acute dermatitis in radiosensitive patient: case study," Radiat. Prot. Dosimet. **182**(1), 93–97 (2018).
14. C. Navarrete-Dechent, M. Cordova, K. Liopyris, S. Aleissa, M. Rajadhyaksha, A. A. Marghoob, A. M. Rossi, and C. A. Barker, "In vivo imaging characterization of basal cell carcinoma and cutaneous response to high-dose ionizing radiation therapy: A prospective study of reflectance confocal microscopy, dermoscopy, and ultrasonography," J. Am. Acad. Dermatol. **84**(6), 1575–1584 (2021).
15. S. Vano-Galvan, E. Fernandez-Lizarbe, M. Truchuelo, B. Diaz-Ley, E. Grillo, V. Sanchez, L. Ríos-Buceta, J. Paoli, S. Sancho, and A. Montero, "Dynamic skin changes of acute radiation dermatitis revealed by in vivo reflectance confocal microscopy," J. Eur. Acad. Dermatol. Venereol. **27**(9), 1143–1150 (2013).
16. A. Hariri, F. Chen, C. Moore, and J. V. Jokerst, "Noninvasive staging of pressure ulcers using photoacoustic imaging," Wound Rep. Reg. **27**(5), 488–496 (2019).
17. Y. Kanemura, M. Kanazawa, S. Hashimoto, Y. Hayashi, E. Fujiwara, A. Suzuki, T. Ishii, M. Goto, H. Nozaki, T. Inoue, and H. Takanari, "Assessment of skin inflammation using near-infrared Raman spectroscopy combined with artificial intelligence analysis in an animal model," Anal. **147**(12), 2843–2850 (2022).
18. A. Bjorgan, M. Milanic, and L. L. Randeberg, "Estimation of skin optical parameters for real-time hyperspectral imaging applications," J. Biomed. Opt. **19**(6), 066003 (2014).
19. A. S. Bernat, F. J. Bolton, K. Bar-Am, S. L. Jacques, D. Levitz, D. Levitz, and A. Ozcan, "Assessing changes in oxygen saturation using a low cost multi-spectral imaging system," Proc. SPIE **10869**, 1086918 (2019).

20. F. J. Bolton, A. S. Bernat, K. Bar-Am, D. Levitz, and S. Jacques, "Portable, low-cost multispectral imaging system: design, development, validation, and utilization," J. Biomed. Opt. **23**(12), 1–11 (2018).

21. S. S. Hao, "Development and performance validation of a low-cost algorithms-based hyperspectral imaging system for radiodermatitis assessment: code," figshare, 2023, https://doi.org/10.6084/m9.figshare.23641065.

22. GarrettTW, "MCML_SimulateSpectroscopy," Github, 2019, https://github.com/GarrettTW/MCML_Simulate Spectroscopy.

23. S. L. Jacques, R. Samatham, and N. Choudhury, "Rapid spectral analysis for spectral imaging," Biomed. Opt. Express **1**(1), 157–164 (2010).

24. S. Prahl, "Optical Absorption of Hemoglobin," (omlc.org, 1999), https://omlc.org/spectra/hemoglobin/.

25. G. M. Hale and M. R. Querry, "Optical constants of water in the 200-nm to 200-µm wavelength region," Appl. Opt. **12**(3), 555–563 (1973).

26. S. L. Jacques and D. J. McAuliffe, "The melanosome: threshold temperature for explosive vaporization and internal absorption coefficient during pulsed laser irradiation," Photochem. Photobiol. **53**(6), 769–775 (1991).

27. C. Y. Wright, A. E. Karsten, M. Wilkes, A. Singh, J. du Plessis, P. N. Albers, and P. A. Karsten, "Diffuse Reflectance Spectroscopy Versus Mexameter((R)) MX18 Measurements of Melanin and Erythema in an African Population," Photochem. Photobiol. **92**(4), 632–636 (2016).

28. C.-J. Huang, M.-F. Hou, K.-H. Luo, S.-Y. Wei, M.-Y. Huang, S.-J. Su, H.-Y. Kuo, S.-S. F. Yuan, G.-S. Chen, and S. C.-S. Hu, "RTOG, CTCAE and WHO criteria for acute radiation dermatitis correlate with cutaneous blood flow measurements," Breast J. **24**(3), 230–236 (2015).